

Two-phase Turbulence Structure in a Microbubble Channel Flow

Atsuhide KITAGAWA*, Koichi HISHIDA** and Yoshiaki KODAMA*

* *Center for Smart Control of Turbulence, National Maritime Research Institute,
6-38-1 Shinkawa, Mitaka, Tokyo 181-0004, Japan*

** *Department of System Design Engineering, Keio University,
3-14-1 Hiyoshi, Kohoku-ku Yokohama, Kanagawa 223-8522, Japan*

The turbulence structure of flow field including microbubbles in a horizontal channel is experimentally investigated using combined particle image velocimetry in order to clarify the mechanism for drag reduction caused by microbubbles. Firstly, a simultaneous measurement system for liquid phase and dispersed bubbles is proposed, which is based on the combination of Particle Tracking Velocimetry, Laser Induced Fluorescence and Shadow Image Technique (PTV/LIF/SIT). Secondly, the measurement techniques for both phases are introduced in detail. To accurately detect the velocity vectors of the liquid phase in the two coexistence phases, only the tracer particles overlapped with bubble shadow images are almost entirely eliminated as a post-processing. Finally, turbulence characteristics of the objective flow field are presented with the measurements for both phases obtained by the proposed system. The bubble deformation effect to the turbulence modification around the bubble is clarified.

1. Introduction

The frictional drag reduction improves transport efficiency of ships since most of the total resistance of large ships is due to skin friction. A number of drag reduction devices which include microbubble technique, riblets, large-eddy-breaking-up devices, and micromachines have been proposed. Particularly, the microbubble technique is applied to large ships such as tankers which have a box shape with a wide and flat bottom. Because when bubbles are injected at bow, the buoyancy of bubbles helps them to stay close to the bottom wall and thus helps them to cover the entire bottom surface efficiently.

Since McCormick and Bhattacharyya (1973) found drag reduction on a submerged body by injecting microbubbles, several researches have reported on microbubble drag reduction. Madavan et al. (1984) performed experiments where microbubbles were injected into a turbulent boundary layer through a porous plate, and showed that the frictional drag reduction caused by microbubbles reaches up to 80 %. Kodama et al. (2000) carried out microbubble experiments using a 50 m-long flat plate ship whose scale is close to that of a full-scale ship at sea, and showed a reduction in both local skin friction and total drag. Deutsch et al. (2003) conducted experiments in the 12-inch diameter tunnel to investigate the effect of surface roughness on the microbubble drag reduction. They showed that the drag reduction effect is larger for larger surface roughness. From these experiments, a marked improvement in the transport efficiency of ships using the microbubble technique is expected. However, the mechanism for the drag reduction is not fully understood yet, mainly because the information on the bubble motion and the local interaction between bubbles and surrounding liquid cannot be sufficiently obtained using pointwise measurement techniques adopted in previous papers.

Recently, several measurement systems implementing image processing techniques have been developed and applied to various bubbly flow fields. Tokuhiro et al. (1998) investigated the flow around an oscillating bubble and solid ellipsoid using the Particle Image Velocimetry (PIV) system with Laser Induced Fluorescence (LIF) and an Infrared Shadow Technique (IST) to obtain the shape of the bubble and solid. They clarified the difference around and in the wake of the bubble and particle. Murai et al. (2000) showed that the energy spectrum of the liquid phase in a two-phase bubbly flow is strongly dependent on the bubble-to-bubble spacing through local measurement with Particle Tracking Velocimetry (PTV) technique. Minato et al. (2003) investigated the turbulence modification in a bubbly pipe flow using PIV/LIF technique, and revealed that a large number of bubbles near the wall disturb the transport of the turbulence energy produced in the wall shear layer. From the above literatures, the image processing technique is considered as a useful tool to clarify the flow structures of two-phase bubbly flows comprehensively.

In the present study, in order to clarify the mechanism of the drag reduction caused by microbubbles, the two-phase turbulence structure of flow field including microbubbles in a horizontal channel is experimentally investigated using the combined particle image technique. The objective flow is hereinafter called microbubble flow. In this paper, the measurement system for both two phases and the technique for the liquid velocity detection with high accuracy are

introduced in Section 2 and in Section 3. Moreover, the two-phase turbulence characteristics in the microbubble flow are presented and discussed in Section 4.

2. Experimental setup

2.1 Experimental apparatus and measurement method

Figure 1 (a) shows a schematic diagram of the experimental apparatus. The liquid circulates through the pump, the electro-magnetic flow meter, the channel (test section), and the dump tank. Air bubbles injected in the channel are removed in the dump tank by its buoyancy, thus allowing continuous operation. The channel is made of transparent acrylic resin with inner dimensions $H \times B \times L = 15 \times 100 \times 3000$ mm. The gas injection device is set at 1028 mm downstream site from the vena contracta. Air bubbles are injected into the channel through an array-of-holes plate (AHP) installed on the upper wall. The AHP has injection area $B_A \times L_A = 72 \times 36$ mm, where 0.25 mm diameter holes are drilled at 3.5 mm spanwise and 5 mm streamwise pitches. The origin of the Cartesian coordinate x (streamwise), y (wall-normal) and z (spanwise) is located at the center of the air injection plate on the upper wall and the y -axis is oriented upward. The test region is set at $x = 500$ mm and $z = 0$ mm.

In the present study, the velocity vectors of the liquid phase and dispersed bubbles are measured by the image processing technique. This technique is described in detail in Section 3. In addition, the LIF is applied in order to settle optical problems such as the light scattered at the bubble interface and the halation generated at the wall of the channel. The fluorescent particles with Rhodamine-B as the fluorescent dye are applied as the tracer particles for the image processing technique. The specific density and the diameter of the particles are 1.03 g/cm^3 and approximately 1-10 μm . The absorption wavelength region of the Rhodamine-B ranges from approximately 460 to 550 nm and that of emission from approximately 550 to 700 nm. The particle concentration in the measurement is approximately 60 ppm. Additionally, Shadow Image Technique (SIT) which was proposed by Tokuhiko et al. (1998), is applied for obtaining both the shape and the location of individual bubbles.

Figure 1 (b) shows the outline of the optical measurement system. This figure illustrates a cross-section view of the channel. In this system, two CCD cameras (Kodak ES1.0, resolution: 1008×1018 pixels) are utilized for performing the measurement of both phases. The horizontal camera (b5) in this figure is used for the measurement of the liquid tracers while the vertical one (b7) is used for the measurement of the bubbles. Nd:YAG laser ($\lambda = 532$ nm) with a pulse intensity of 25 mJ and LED array ($\lambda = 850$ nm) are applied as light sources for the measurements of each phase, respectively. The laser light sheet with thickness of about 1.0 mm is emitted from the lower part of the channel at $z = 0$ while the infrared light is emitted from the upper part of the channel. The emitted lights are reflected upward through the mirror installed on the upper wall of the channel. The size of the mirror is 15 mm in length, 9 mm in breadth and 1.5 mm in thickness, respectively. The angle between the mirror and the upper wall is 45 deg. The gap distance between the mirrors is 20 mm in minimum. To separate the visible and infrared lights, the cold mirror (Sigmakoki CLDM-50S) which reflects the visible light and transmits the infrared light, is utilized. Furthermore, the fluorescent particle images are captured through a cutoff filter ($\lambda = 550\text{-}720$ nm; $T > 95\%$, $\lambda = 532$ nm; $T < 0.03\%$, $\lambda = 815\text{-}885$ nm; $T < 0.01\%$) to cut off the high intensity light reflected from the bubble interface. The trigger timings of the laser, the LEDs and the two CCD cameras are synchronized using a pulse generator. The images taken through a CCD camera system with a frame rate of 30 fps are directly ported to PC s. The original images are digitized through an image capture board. The field of view is $15.0 \text{ mm} \times 6.0 \text{ mm}$ and the spatial resolution is 0.016 mm/pixel. The experimental conditions are shown in Table 1. The tap water with contaminants removed by filtration is applied as the working fluid. The bulk velocity of the liquid U_m is 5 m/s. The bulk Reynolds number Re_m based on U_m and the channel half height h is approximately 41200. The mean bubble diameter Da is approximately 0.53 mm. The void fraction α in this table is defined as

$$\alpha = \frac{Q_G}{Q_G + Q_L}, \quad (1)$$

where, Q_L and Q_G stand for the liquid flow rate and the gas flow rate, respectively.

2.2 Effect of mirror to the flow field

In the present system, we feel apprehensive about the effects of mirrors to the flow structure because the two mirrors

are installed inside in the channel. Therefore, the displacement thickness δ^* on the mirror and the fluctuation scale of the turbulence in the spanwise direction w' are roughly estimated. The displacement thickness δ^* is estimated as

$$\delta^* = 0.37x_M \left(\frac{U_m x_M}{\nu} \right)^{-1/5}, \quad (2)$$

where, U_m is the mean liquid velocity, x_M is the streamwise length of the mirror (= 15 mm) and ν is the kinematic viscosity of the liquid. Consequently the displacement thickness δ^* at the end of the mirror is approximately 0.6 mm in the case of $U_m = 5.0$ m/s. In addition, the fluctuation scale in the spanwise direction w' which is estimated by DNS results for $Re = 13800$ (Kim et al., 1987) is approximately 0.9 mm. Therefore, the effect of mirrors to the flow field is considered negligible because the minimum separation distance between the mirror and the test region in the present system is approximately 10 mm.

3. Measurement technique

3.1 Technique for liquid phase velocity detection

One of the advantages of the measurement using the image processing technique is that the simultaneous measurement of the two phases can be easily conducted by combining image processing techniques. For the measurement of turbulent flow including a large number of bubbles, e.g. microbubble flow, PTV technique is considered more suitable as an image processing technique compared to PIV technique. This is because in the PIV liquid velocity vectors with high accuracy cannot be detected with increasing void fraction. This originates from the decrease of the gap area among bubbles related to the interrogation area and the increase of the liquid fluctuation velocities induced in the bubble wake. For this reason, we measure the velocity of the liquid phase using the PTV technique. The image processing method adopted for the PTV technique is based on a velocity gradient tensor (VGT, in abbreviation) algorithm developed by Ishikawa et al. (2000). The procedures of the measurement for the liquid phase are as follows (see Fig. 2 (a)):

1. By using particle mask correlation (PMC), the centroid of each fluorescent tracer particle is calculated from the original images taken with CCD camera.
2. The velocity vectors of individual fluorescent tracer particles are calculated by VGT with a time separation of 26 μ s between a pair of images.

We suspect that erroneous vectors are included in velocity vectors in the vicinity of the bubble interface because the flow field in the present study is turbulent flow with a large number of bubbles. Therefore, the fluctuation velocity of the tracer particle which is more than the threefold RMS value of the velocity, is regarded as the erroneous vector. Regarding the mean liquid velocity in the streamwise direction, consequently, the relative error of the present data to LDV measurement is approximately 2.5 % in maximum.

3.2 Technique for bubble velocity detection

Some available techniques for calculating the centroid of the bubble have been proposed, e.g. a binary labeling method and a template matching method. Here, the binary labeling method can treat the deformation of the bubble but cannot treat the overlapping bubble. In contrast, the template matching method can treat the latter but cannot treat the former. In the present study, the binary labeling method is adopted from the perspective of the efficiency of the working time although in the microbubble flow a large number of bubbles overlap as well as the deformation of bubbles is remarkable. Consequently, the in-focus overlapping bubbles are not considered. The procedures of the measurement for the bubbles are as follows (see Fig. 2 (b)):

1. The average brightness of the images obtained by the SIT is adjusted to emphasize the edges of the bubbles. Then only the focused bubbles are extracted.
2. The brightness of the images is inverted for easy handling of the process below. The centroids of the bubbles are then calculated from the images which are binarized using the method proposed by Otsu (1979). Here, in this method, a threshold is determined by the histogram of the brightness in the image.
3. The velocity vectors of the bubbles are calculated by the two-time-step tracking method.

In this study, the bubble diameter is calculated as the equivalent diameter from the constituent pixel number of individual bubble. The equivalent diameter D of individual bubbles ranges from 10 to 60 pixels. The displacement of the centroids of the bubbles is 7-13 pixels per frame. According to our analysis with artificial bubble images, the error for the displacement of the centroid of the bubble is around 0.1 pixel for $D = 10$ pixel. Consequently, it is estimated that the uncertainty of the bubble velocity vector accompanied by the detection of the centroid of the bubbles is approximately within 2.9 %.

3.3. Elimination method of the tracer particle overlapped with bubble shadow image

The treatment of the tracer particles overlapped with bubble shadow images is one of the essential issues for the liquid velocity detection in the microbubble flow. Such a tracer particle is hereinafter called overlapping particle, for the sake of convenience. For instance, the velocity of the bubble interface is detected by the PTV technique when the fluorescent tracer particle attaches to the bubble. In contrast, the erroneous liquid fluctuation velocity is detected when bubbles exist between the camera and test region, because the fluorescent light from particles is refracted at the bubble interface. In this paper, the available method for eliminating the overlapping particles is introduced in order to detect only the liquid velocity in the microbubble flow accurately, because we cannot completely eliminate overlapping particles by using only the correlation coefficient in the PTV technique. The procedures of the elimination method are as follows:

1. The average brightness of the images of the bubbles is adjusted.
2. The center region of the bubble where becomes a hollow is recognized as the bubble.
3. Only the particles overlapped with the binarized bubble image are eliminated.

4. Results and discussions

4.1. Skin friction coefficient

Figure 3 indicates the skin friction coefficient measured by the experimental apparatus described in Section 2. In this figure, the horizontal axis is the bulk void fraction while the vertical axis is the ratio of the skin friction coefficient in the bubbly flow C_f to that in single-phase flow C_{f0} . The skin friction coefficient C_{f0} is given by

$$C_{f0}(Q_G) = C_{f0}(0) \frac{\tau[U(Q_G)]}{\tau[U(0)]}, \quad (3)$$

where, $U(Q_G)$ is the mean liquid velocity at Q_G and τ is the wall shear stress estimated by the empirical Blasius formula. That is, C_{f0} is corrected for the blockage effect as a function of the gas flow rate (see Kodama et al. 2000). It is clear that the ratio of the skin friction coefficient reduces with increasing void fraction. It is also clear that the drag reduction effect is approximately 2.5 % when the void fraction is 0.5 %, which is the present experimental condition.

4.2. Simultaneous measurement data obtained by PTV/LIF/SIT system

Figure 4 indicates the measured result at $\alpha = 0.5$ %. In this figure, the white (or gray) and yellow regions are the bubble shadow images and in-focus bubble shadow images obtained by the SIT, respectively. The arrows stand for the liquid velocity and the velocity of in-focus bubbles. The upper part of the image corresponds to the upper wall of the channel. It is observed that liquid velocity vectors around individual bubbles and the velocity vectors of in-focus bubbles can be obtained relatively well. In addition, no overlapping particles can be observed. It is therefore expected that the two-phase turbulence characteristics in the microbubble flow are sufficiently obtained using the proposed measurement system.

4.3. Microbubble flow characteristics

To obtain the detailed information on the turbulence structures in the microbubble flow, statistical analysis of the data for both the liquid phase and the bubble is performed. The number of grid divisions is 32 and the grid spacing is approximately 0.176 mm. The sampling number with respect to the liquid phase is more than 5000 in each grid element. Regarding the bubble, only the data that has more than 200 sampled number per one grid element is indicated.

Figure 5 shows the mean velocity profile of liquid phase and the bubble at $\alpha = 0.5\%$. The horizontal axis is the distance from the upper wall of the channel normalized by the channel half-height h . In this figure, u and v represent the mean velocities in the streamwise and wall-normal directions and the subscript L and G are the liquid phase and the bubble, respectively. It is clear that the liquid velocity profile is almost the same with the bubble velocity profile. It is expected that this tendency has validity, because the bubble response time with the diameter of 0.5 mm is much less than 0.1 s and in the test region the bubble must follow the mean liquid velocity. Figure 6 shows the turbulence intensity profile of the liquid phase and the bubble, which is normalized by u_C . Here u_C is the maximum velocity of the single liquid phase at the center of the channel ($y = h$) and is approximately 5.82 m/s. In this figure, u_{rms} and v_{rms} represent the turbulence intensities in the streamwise and wall-normal directions, respectively. It is clear that the liquid turbulence intensity in the streamwise direction decreases slightly in a few regions while that in the wall-normal direction decreases slightly in the whole region, by injecting bubbles. It is also clear that the difference of the turbulence intensities between liquid phase and the bubble is larger as the normalized distance from the wall is shorter. It is expected that this results from that in the vicinity of the wall the liquid motion with small scale does not affect sufficiently to the bubble motion. Figure 7 shows the profiles of the Reynolds stress of the liquid phase and the correlation of the bubble fluctuation velocities, which are normalized by u_C^2 . It is obvious from this figure that the Reynolds stress decreases in the whole region by injecting bubbles. This leads the wall shear stress to decrease, whereby it is directly connected to the frictional drag reduction. It is also obvious that the correlation of the bubble fluctuation velocities is much smaller than the Reynolds stress of the liquid phase. Namely, the bubble's translational motion is remarkably different from the surrounding liquid turbulence motion.

4.4. Bubble deformation effect

In this section, the bubble deformation effect to the turbulence modification around the bubble is investigated to clarify the mechanism of the decrease of the Reynolds stress. Figure 8 shows the consecutive images of the in-focus bubble in the vicinity of the upper wall of the channel, which was taken with a high-speed camera (IDT, X Stream XS-3, resolution: 1024×640 pixels.). The shutter speed of the camera is 1/50000 s and the frame rate is 3750 fps. From the figure, it is well observed that the degree of the deformation and the inclination angle of the bubble vary significantly as the time elapses. Figure 9 and 10 show the relations of the bubble equivalent diameter D and the bubble inclination angle θ to the bubble deformation ratio γ , which is defined as

$$\gamma = \frac{L - D}{D}. \quad (4)$$

Where, L is the length of the longer axis of the bubble assuming an ellipsoidal shape. The schematic definition of θ and γ is illustrated in each figure. θ is set to positive on the upper wall side. Each data is an averaged-value over the bubbles inside each region, i.e., $|y|/h = 0.1-0.2, 0.2-0.3$ and $0.3-0.4$. It is clear from figure 9 that γ becomes large as D is larger and the distance from the upper wall is shorter. From figure 10, it is clear that γ varies with θ and that in all $|y|/h$ regions γ is the largest when θ ranges from -60 to -30 degrees.

To clear the turbulence modification due to the local liquid-bubble interaction, the frequency of the occurrence of negative $u'_L v'_L$, η , is calculated. The domain of detecting the $u'_L v'_L$ in proximity to the in-focus bubble is defined in figure 11(a), in which La is the half-length of L . Xa and Ya are, respectively, the lengths of the domain in the streamwise and the wall-normal directions and Ya is set to La . η is defined as N_I/N_T , where N_I is the detection number of the negative $u'_L v'_L$ around the in-focus bubble and N_T is the sampling number (see Fig. 11 (b)). Note that in the case of the present co-ordinate system the Reynolds stress on the upper wall side decreases with increasing η . Figure 12 shows the calculated frequency averaged at $|y|/h = 0.1-0.2, 0.2-0.3$ and $0.3-0.4$. The “infinity” in this figure means that $Xa \rightarrow \infty$. It is clear that in all $|y|/h$ regions η increases with decreasing Xa . This indicates that the turbulence around the bubble has a tendency to become isotropic. It is therefore expected that the increase of the bubble number density makes the turbulence over wide range isotropic. This corresponds to the previous measurement that the frictional drag reduces with increasing void fraction. Figure 13 indicates the relationship between the bubble deformation ratio γ and the frequency of the occurrence of negative $u'_L v'_L$, η , at $Xa = 4La$ and $Ya = La$. From this figure, it is obvious that in all $|y|/h$ regions η becomes large as γ is larger. This means that the bubble deformation contributes to the isotropy of the turbulence, which causes the decrease of the Reynolds stress. The reason of the decrease of the Reynolds stress due to

the bubble deformation is explained as follows: The longer axis of the bubble with large deformation tends to be in parallel with the axis of the distortion of the mean liquid velocity, as shown in figure 10. Under this situation, the liquid in proximity to the deformed bubble has a same direction as the longer axis because it currents along the bubble interface, whether the relative velocity between the surrounding liquid and the bubble is positive or not (see Figs. 13 (a) and (b)). Consequently, the correlation between u'_L and v'_L around the bubble with the inclination angle raging from -30 to -60 degrees is consistently negative. The generated negative $u'_L v'_L$ contributes directly to the isotropy of the turbulence. Note that the $u'_L v'_L$ around the bubble becomes positive when θ ranges from 30 to 60 degrees, however, the frequency and the deformation ratio of its bubble are quite low (see Figs. 10) and its effect is hardly appeared.

From above results, it was found that the decrease of the Reynolds stress is relevant to the bubble deformation. In the future, we should carry out an investigation on the bubble deformation effect in detail to comprehensively clarify the mechanism of the frictional drag reduction due to microbubbles.

5. Conclusions

The turbulence structure of the microbubble flow in the horizontal channel was experimentally investigated using the image processing technique, in order to clarify the mechanism of the drag reduction caused by microbubbles. Under the conditions that the bulk void fraction is approximately 0.5%, the concluding remarks have been revealed for the present study.

1. A simultaneous measurement system based on the combination of Particle Tracking Velocimetry, Laser Induced Fluorescence and Shadow Image Technique (PTV/LIF/SIT) was proposed and the velocity vectors of the liquid phase and bubbles were succeeded in detecting simultaneously. In addition, the fluorescent tracer particles overlapped with the bubble shadow images were almost entirely eliminated in order to detect the liquid velocity vectors accurately.
2. The mean liquid velocity is almost consistent with the mean bubble velocity.
3. The liquid turbulence intensity in the streamwise direction decreases slightly in a few regions while that in the wall-normal direction decreases slightly in the whole region, by injecting bubbles. In addition, the difference of the turbulence intensities between liquid phase and the bubble becomes large as the normalized distance from the wall is shorter.
4. The Reynolds stress of the liquid decreases in the whole by injecting bubbles. This relates directly to the frictional drag reduction. The correlation of the bubble fluctuation velocities is much smaller than the Reynolds stress of the liquid phase.
5. The decrease of the Reynolds stress is relevant to the bubble deformation.

Acknowledgement

This work was carried out as a research activity at the Center for Smart Control of Turbulence funded by the Ministry of Education, Culture, Sports, Science and Technology, Japan. We would also like to thank Dr. Sugiyama at National Maritime Research Institute and Dr. Fujiwara at the University of Tokyo for their comments on the manuscript of this paper.

Reference

- Deutsch, S., Moeny, M., Fontaine, A., Petrie, H., 2003. Microbubble drag reduction in rough walled turbulent boundary layers, Proc. ASME-JSME FED Joint Conf./CD-ROM, Paper No.FEDSM2003-45647, 1-9.
- Ishikawa, M., Murai, Y., Wada, A., Iguchi, M., Okamoto, K., Yamamoto, F., 2000. Novel algorithm for particle tracking velocimetry using the velocity gradient tensor, Experiments in Fluids, 29-6, 519-531.
- Kim, J., Moin, P., Moser, R., 1987. Turbulence statistics in fully developed channel flow at low Reynolds number, J. Fluid Mech., 177, 133-166.
- Kodama, Y., Kakugawa, A., Takahashi, T., Kawashima, H., 2000. Experimental study on microbubbles and their applicability to ships for skin friction reduction, Int. J. Heat and Fluid Flow, 21, 582-588.
- Madavan, N.K., Deutsch, S., Merkle, C.L., 1984. Reduction of turbulent skin friction by microbubbles, Phys. Fluids, 27, 356-363.

McCormick, M.E., Bhattacharyya, R., 1973. Drag reduction of a submersible hull by electrolysis, *Nav. Eng. J.*, 85, 11-16.

Minato, D., Tanaka, T., Fujiwara, A., Hishida, K., Maeda, M., 2003. Particle tracking velocimetry measurement of bubble-bubble interaction, *Proc. ASME-JSME FED Joint Conf./CD-ROM*, Paper No. TED-AJ03-198.

Murai, Y., Song, X. Q., Takagi, T., Ishikawa, M., Yamamoto, F., Ohta, J., 2000. Inverse energy cascade structure of turbulence in a bubbly flow (PIV measurement and results), *JSME International Journal, Series B (Fluids and Thermal Engineering)*, Vol. 43, No. 2, 180-187.

Otsu, N., 1979. A threshold selection method from gray-level histograms. *IEEE Trans. Sys., Man, and Cybernetics*, SMC-9. 1, 62-66.

Tokuhiro, A., Maekawa, M., Iizuka, K., Hishida, K., Maeda, M., 1998. Turbulent flow past a bubble and an ellipsoid using shadow-image and PIV techniques, *Int. J. Multiphase Flow*, 24,1383-1406.

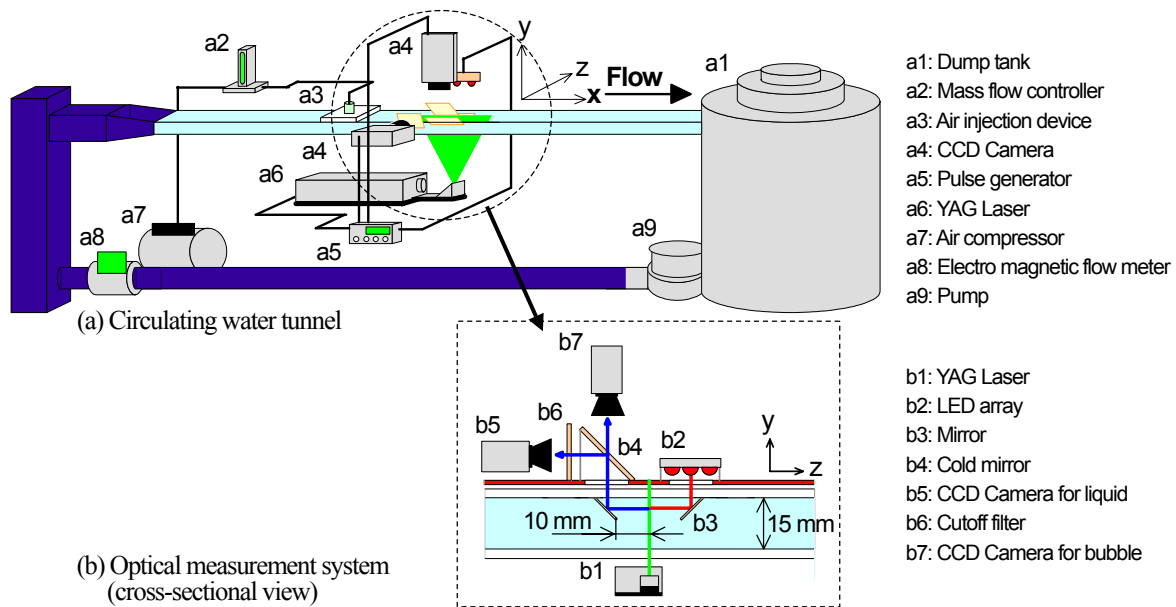
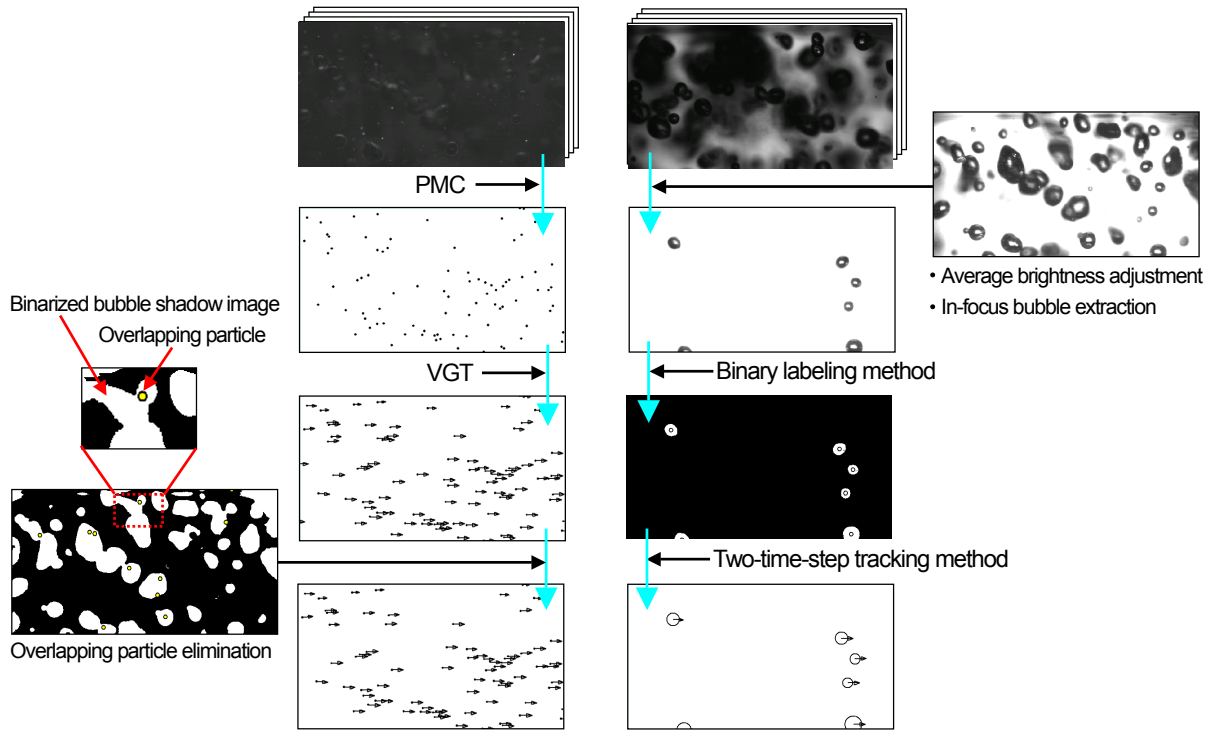


Fig.1 Schematic diagram of experimental apparatus

Table 1 Experimental conditions

Channel size	3000mm × 15 mm × 100mm
Temperature of liquid	24.0~25.0 °C
Kinematic viscosity of liquid	$\nu = 0.91 \times 10^{-6} \text{ m}^2/\text{s}$
Channel half height	$h = 7.5 \text{ mm}$
Bulk liquid velocity	$U_m = 5.0 \text{ m/s}$
Bulk Reynolds number	$Re_m = h \cdot U_m / \nu = 41200$
Bulk void fraction	$\alpha = 0.5 \%$
Mean bubble diameter	$Da = 0.53 \text{ mm}$



(a) Liquid velocity detection (b) Bubble velocity detection

Fig.2 Flow chart of the image processing for liquid and bubble velocity detections

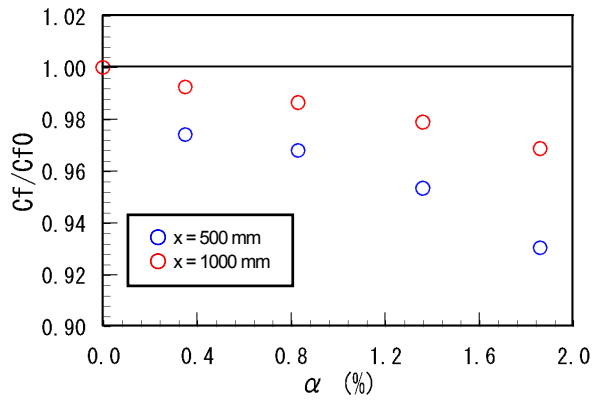


Fig.3 Ratio of skin friction coefficient in bubbly flow to that in single phase flow in the case of $U_m = 5.0$ m/s

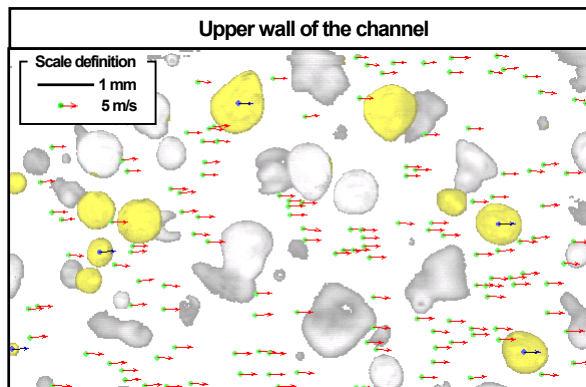


Fig.4 PTV/LIF/SIT result at $\alpha = 0.5\%$

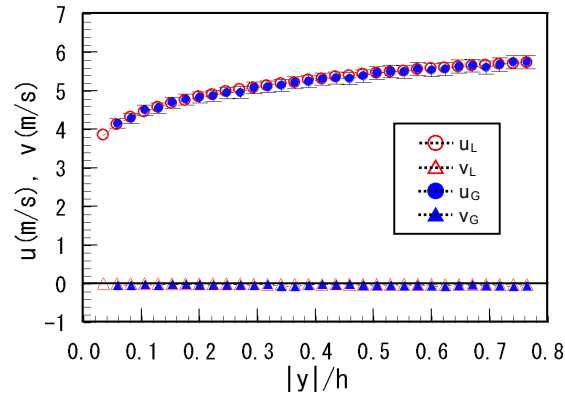


Fig.5 Mean velocity profile of liquid phase and bubble at $\alpha = 0.5\%$

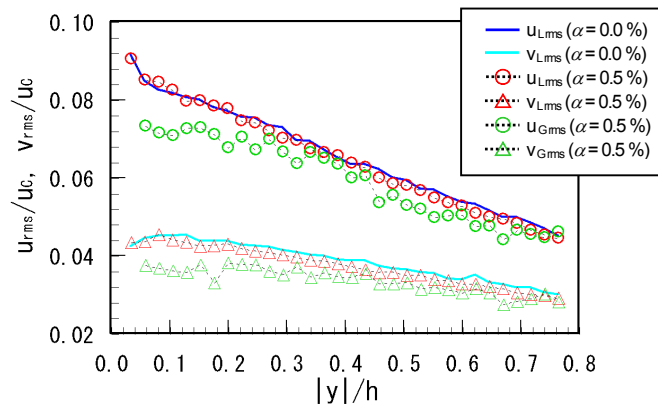


Fig.6 Turbulence intensity profile of liquid phase and bubble

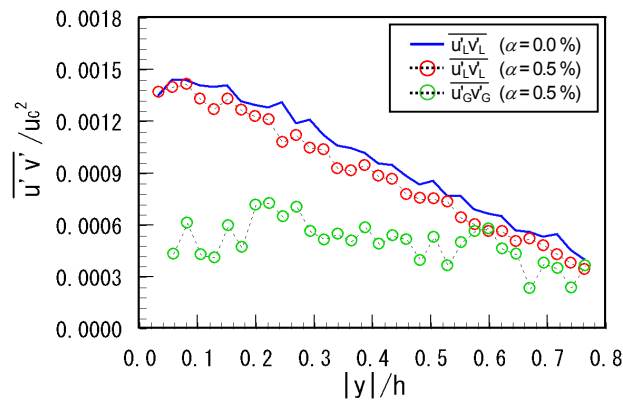


Fig.7 Profiles of Reynolds stress of liquid phase and correlation of bubble fluctuation velocities

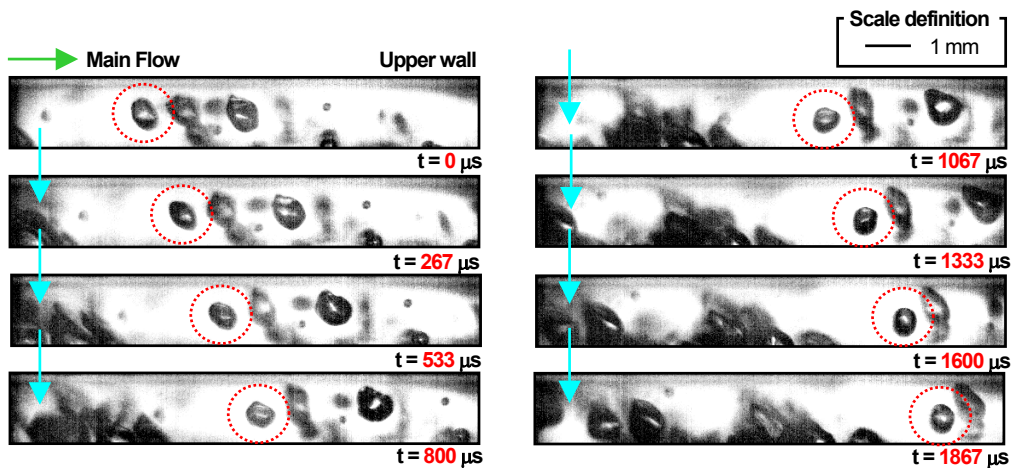


Fig.8 Bubble motion in the vicinity of the upper wall of the channel

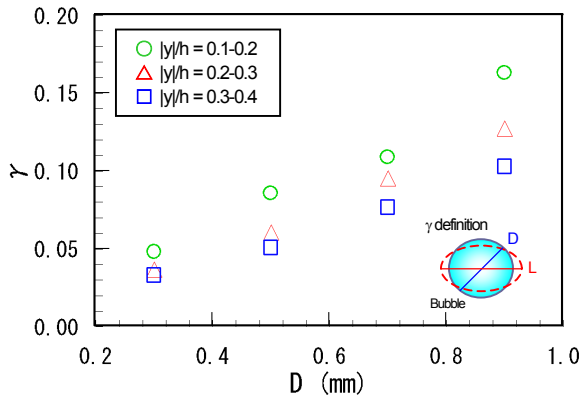


Fig.9 Relationship between equivalent bubble diameter and bubble deformation ratio

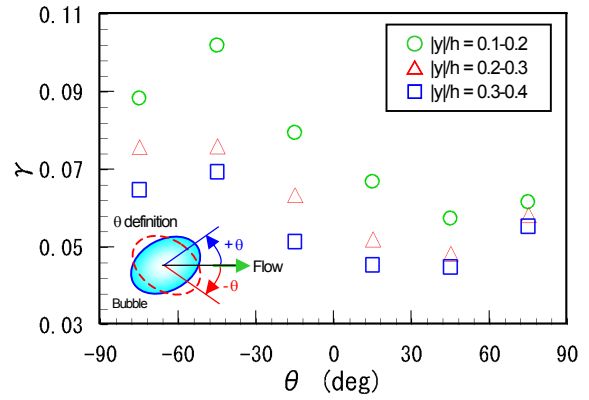


Fig.10 Relationship between bubble inclination angle and bubble deformation ratio

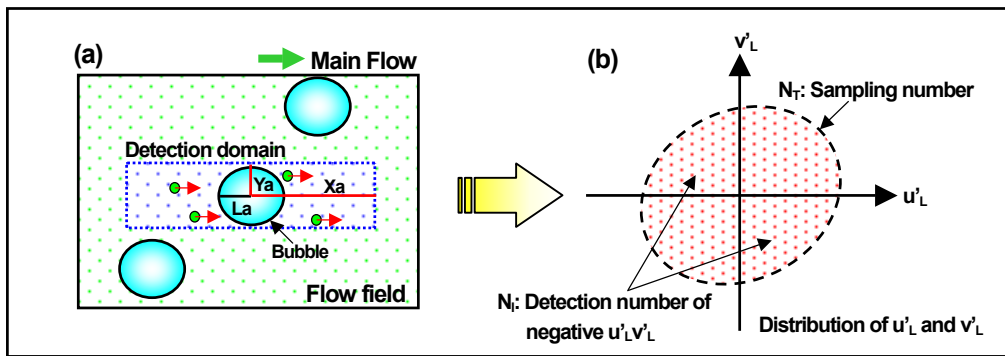


Fig.11 Schematic explanation for calculating the frequency of the occurrence of negative $u'_L v'_L$

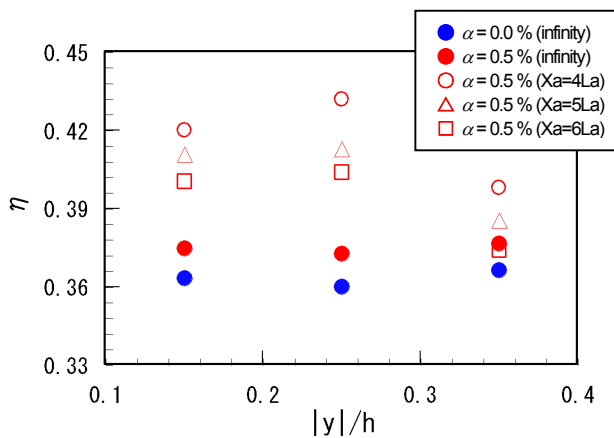


Fig.12 Frequency of the occurrence of negative $u'_L v'_L$ at $Y_a = L_a$

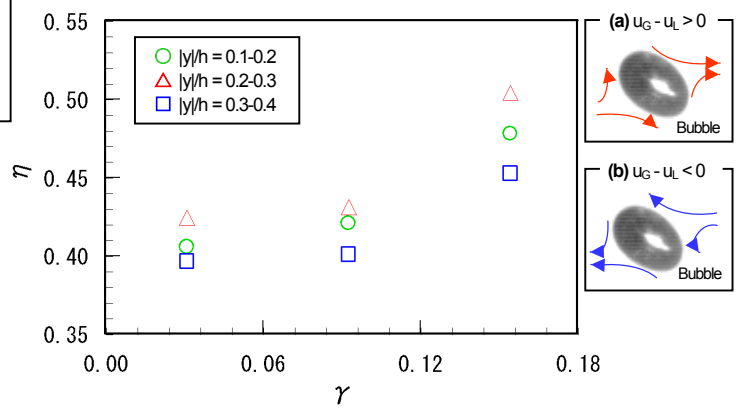


Fig.13 Relationship between bubble deformation ratio and frequency of the occurrence of negative $u'_L v'_L$ at $X_a = 4L_a$ and $Y_a = L_a$